

Article

Strain Engineering of the CeNi₅ System

Ian Shuttleworth

School of Science and Technology, Nottingham Trent University, Nottingham NG11 8NS, UK;
ian.shuttleworth@ntu.ac.uk; Tel.: +44-(0)115-848-3341

Academic Editors: Kevin Bernot and Carlos J. Gómez García

Received: 16 August 2016; Accepted: 19 October 2016; Published: 1 November 2016

Abstract: The effect of strain on the CeNi₅ system has been investigated using density functional theory (DFT). The studies have shown that localised Ce 4f and Ni 3d states carry the magnetic moment of the material. The Ce 4f moment remains relatively unchanged during strain whereas the Ni 3d moment increases as the strain becomes increasingly tensile in both the basal and non-basal directions. A significant strain-dependent interaction exists between delocalised, non-magnetic Ce 6s–Ni 4s states. A weaker group of Ni 3d–Ce 6s/Ni 4s and Ni 3d–Ni 3d interactions exist, indicating that competing localised and delocalised mechanisms act on the Ni 3d states during strain.

Keywords: intermetallic; CeNi₅; strain engineering; lanthanide; RKKY

1. Introduction

Intermetallic compounds have attracted considerable interest because of both their technological versatility and the range of fundamental phenomena that they exhibit. RNi₅ materials—where R is a Y, La, or a rare earth element—are used extensively in Ni–M–H energy storage units, reflecting the wider interest in the use of intermetallic materials in this technology [1].

CeNi₅ has a CaCu₅-type structure with a lattice parameter $a = 4.87 \text{ \AA}$ and a ratio of non-basal to basal dimension of 0.83 [2]. The structure has space group P6/mmm. Investigations of CeNi₅ [3,4] have shown that the local Ce and Ni spin densities are separable, but recent studies into the pressure dependence of the system [5] have highlighted the limitations of a simplistic Stoner model of the magnetic susceptibility of the system. The same study [5] also demonstrated for the contemporary YNi₅ system that a complex set of interactions exists between the spin and orbital moment. It has also been shown that CeNi₅ demonstrates spin fluctuations [6–8], which themselves are an interpolative model [9] that bridges the weakly and strongly ferromagnetic limits.

The magnetic description of CeNi₅ is consequently complex and the current work aims to elucidate the interactions within the bulk crystal by systematically deforming the crystal looking at its response. This technique is conceptually similar to the strain engineering, which has been an important component of semiconductor physics for a number of years [10]. The technique has proven successes, and extensive studies exist of Si, Ge, and III-V alloy systems [11,12]. In addition, recent studies have investigated wide-bandgap materials such as SiC [13]. These studies have a considerably developed understanding of the electronic nature of the materials. Studies of strain across intermetallic materials have shown a greater focus towards their mechanical behaviour and are predominantly applied investigations. Unprecedented studies in surface science [14], however, have used the technique to identify phase transitions in the H/Pt(111) system. The studies have shown that only a nominal change in the Pt(111) surface lattice parameter can cause a shift in the binding position of the surface hydrogen and have demonstrated the utility of strain in fundamental investigations of non-semiconducting systems. The application of [14] is of key importance for the energy industry, as strained Pt overlayers formed across a Pt₃Ni substrate are significantly more catalytically active in the oxygen reduction reaction (ORR)—a key step in energy storage technology—than their unstrained

counterparts [15]. This observation is particularly germane in the current studies: The importance of intermetallic compounds in energy storage has already been identified, and a systematic knowledge of their behaviour under strain may suggest optimal engineering strategies for these materials.

The current work is laid out in the following way: The theoretical techniques are outlined, and a discussion of the results obtained from these techniques is then presented. The results focus on the real space models of the CeNi₅ system and will discuss the spin density, the density of states, and the crystal orbital overlap population (COOP) of the electronic states within the bulk system. The work will then conclude with a summary of the key findings.

2. Theory

The SIESTA LCAO-DFT package [16] was used to perform the simulations presented in this paper. The exchange–correlation interaction was estimated using the revised PBE functional [17]. The atomic orbitals were described using double zeta orbital basis sets [18] and were composed of Ni 3d and 4s orbitals with Ni 4p polarization states, and Ce 4f and 6s orbitals with Ce 6p polarization states. Relativistic pseudopotentials for Ni and Ce were generated using valence configurations of 4s²4p⁰3d⁸4f⁰ and 6s²6p⁰5d¹4f¹, respectively, and using the improved Troullier–Martins method [19,20]. A single Kleinman–Bylander projector was used to represent each angular momentum channel [21]. Brillouin zone integration was performed using an optimal mesh with a fineness of 25 Å [22], and a plane-wave cut-off energy of 300 Ry was used. The GGA method was employed without Hubbard correction because of the Stoner-like character of the system [23]. All calculations presented in this paper were fully spin-polarized. A linear mixing strategy was used to combine the working density matrices during the self-consistency stage of the calculation. A low mixing weight (<1%) was used during this part of the calculation in a strategy that has been proven to reliably generate the ground magnetic state in recent studies of Ce/Pd surface alloys [24].

Figure 1 shows the CeNi₅ unit cell used throughout the current work. The dimensions of the unit cell are defined by the diagonal length parameter a where

$$a_1 = a_2 = \frac{\sqrt{3}}{2}a. \quad (1)$$

The non-basal dimension is defined by c . Throughout this paper, c is presented in units of a ; using this definition, the product ca is in units of Å. During each simulation, the a and c were held constant, and the self-consistent field for that particular system was determined. The ion cores were kept fixed at their P6/mmm sites for every simulation, and no relaxation of the ion core position was performed.

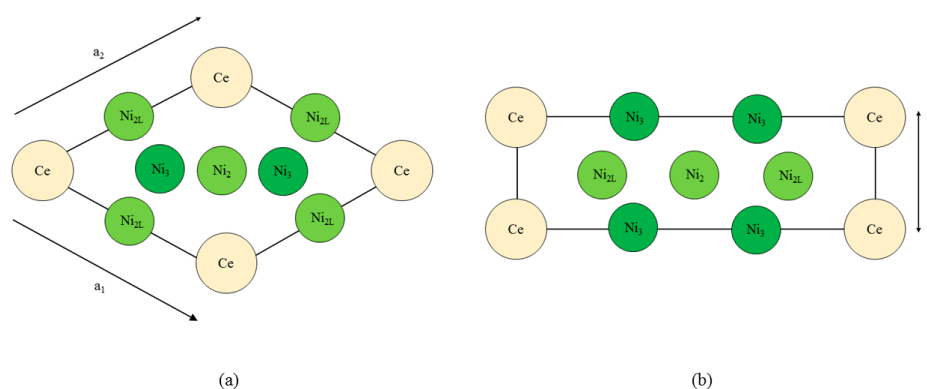


Figure 1. The CeNi₅ structure, (a) projected into the basal plane and (b) in a cross section along the diagonal of the basal plane. The Ce and Ni₃ atoms are at height $c = 0$, whereas the Ni₂ and Ni_{2L} atoms are at a height of $c/2$. The subscripts '2' and '3' refer to the local symmetry of the Ni atoms, and the 'L' highlights the proximity of the Ni atom to the lanthanide.

The spin populations δq were determined using

$$\delta q = q_{\uparrow} - q_{\downarrow}. \quad (2)$$

The q_{\uparrow} and q_{\downarrow} were, respectively, the spin-up and spin-down components of the atomic charge. All results presented in the current work were from a Mulliken population analysis; estimations of the same parameters using both the Hirshfeld [25,26] and Voronoi [26,27] populations were not significantly different to the Mulliken analysis and are consequently not presented. In the current work, the bond orders (BO) were defined as the integral of the crystal orbital hamiltonian population (COHP) [28] up to the Fermi energy E_F [29]. The COHP is closely related to the crystal orbital overlap population (COOP), but the COHP is a partition of the systems band structure energy rather than the electrons. The BO presented in this work should be interpreted as a measure of the relative interaction strength rather than as a direct measure of the amount of electron sharing between orbitals.

Using this formulation, the bond order (BO) can be interpreted as the RKKY interaction [24] using

$$BO = -J^2 \frac{\sin(2k_F r) - 2k_F r \cos(2k_F r)}{(k_F r)^4} \quad (3)$$

where k_F is the Fermi wave-vector, r is the inter-nuclear distance, and J is the interaction strength between spins. The inter-nuclear distances are defined by parameter a in Equation (1) and took values of 4.3–4.8 Å. Based on this length range, the $\sin(2k_F r)$ term predicts a ferromagnetic interaction between the Ni and Ce states, which is seen in the following section.

3. Results and Discussion

Figure 2 shows the equations of state obtained for the bulk CeNi₅ system. The system has been strained by $\pm 5\%$ of the equilibrium lattice parameter; within this range, the Kohn–Sham energies E_{KS} are seen to change by 200–300 meV. Pedagogically, the strain is therefore adequate to evidence changes in the dipole moment, densities of states, and bond order, which will be the focus of the remainder of this work. However, this range of strain would also be accessible experimentally by either changing the stoichiometry of the unit cell by depositing the sample on a support with a different lattice constant—and then particularly studying the interface region between the CeNi₅ and the support—or by applying mechanical strain. Additionally, an applied pressure of up to 7.17 GPa can be used to effect a 5% change in the lattice parameter [30].

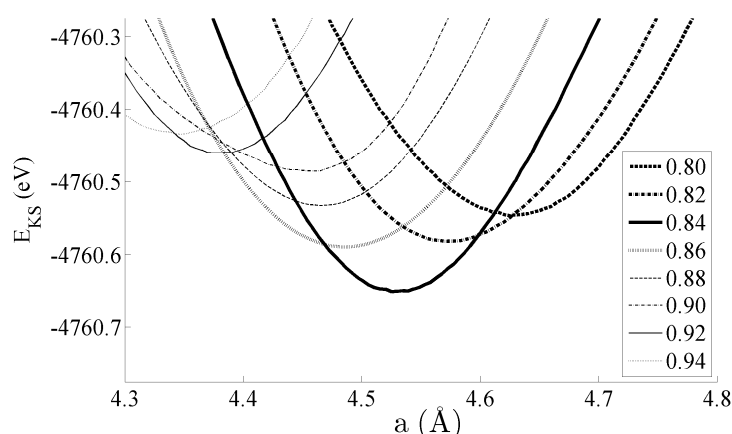


Figure 2. Equations of state for the bulk CeNi₅ system. The inset shows the values of c used for each curve, and the lowest E_{KS} state exists at $a = 4.55$ Å and $c = 0.84$ (3.822 Å).

Figure 3 shows the spin populations δq of the (a) Ce 6s, (b) Ce 4f, (c–e) Ni 4s, and (f–h) Ni 3d states evaluated across the range of strains defined in Figure 2. The results are shown for each of the different types of Ni species present in the unit cell—that is, Ni₃, Ni₂, and Ni_{2L}. Because of their different binding geometries and local symmetry, the electronic character of each of these species is anticipated to be different, particularly between the twofold Ni₂ and Ni_{2L} atoms and threefold Ni₃ atom. The similarities between each of these species and their response under strain will therefore be scrutinised in this work.

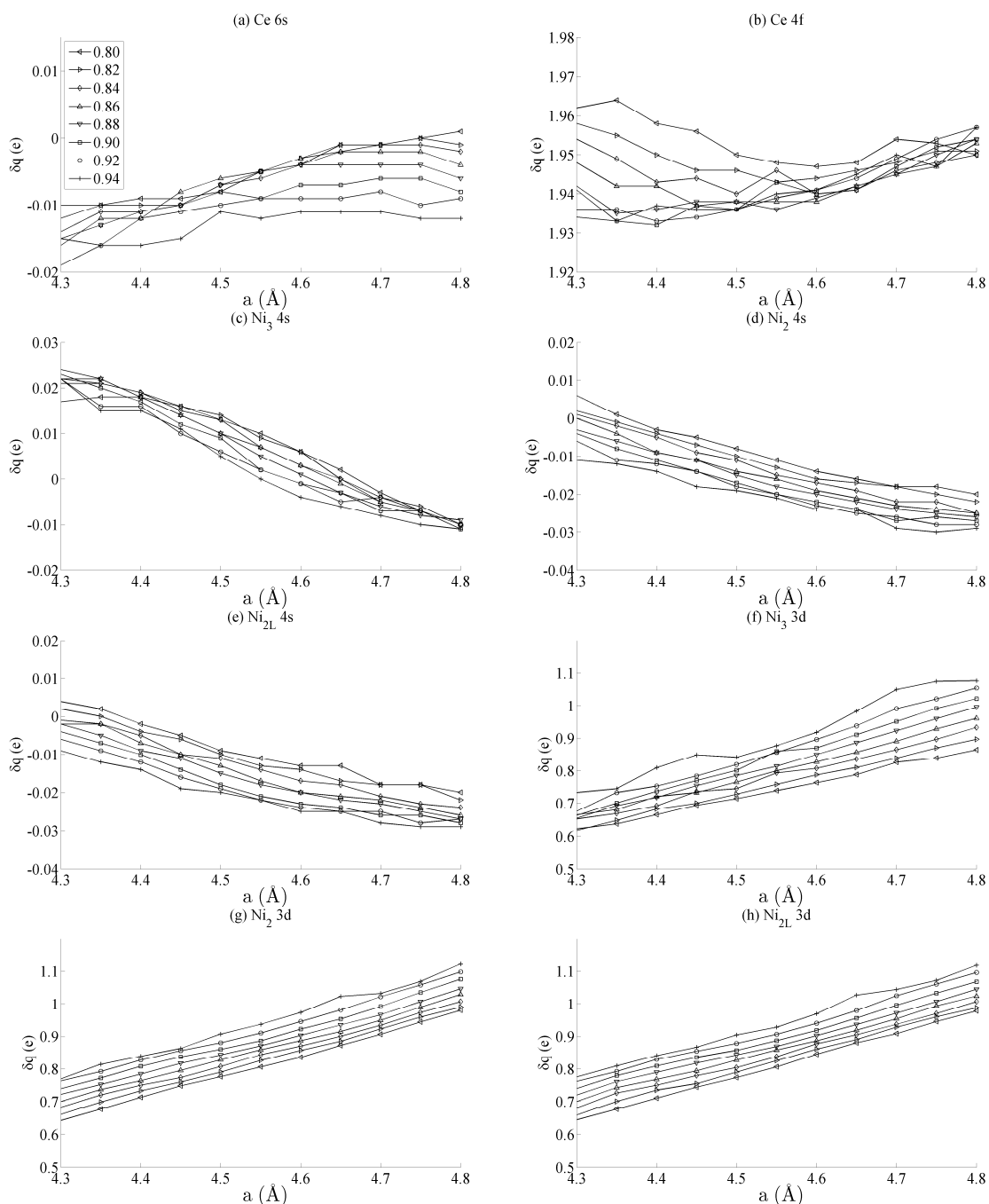


Figure 3. The effects of strain on the spin moment δq of the bulk CeNi₅ system for the (a) Ce 6s, (b) Ce 4f, (c–e) Ni 4s, and (f–h) Ni 3d states. The legend in (a) shows the values of c used for each curve, and the same legend applies to every panel in this figure.

The delocalised Ce 6s and Ni 4s states have δq , which is comparatively negligible to the Ce 4f and Ni 3d states. In addition, the variation in the moment of the Ce 4f state is much smaller than that of any of the Ni 3d states. The variation in the Ce 4f moments shown in Figure 3b is approximately 0.035e. This is over an order of magnitude smaller than the variations of approximately 0.400e seen for the Ni 3d states in Figure 3d–f. The polarizability of each of the Ni 3d states is therefore much larger than that of the Ce 4f states under the influence of strain.

Figure 3d–f also shows that the rate at which δq changes with a —i.e., the slope of the curves shown in those figures—are generally the same for each of the Ni species, particularly for the Ni₂ and Ni_{2L} pair. Certain exceptions exist for the Ni₃ case, particularly for large out-of-plane strains ($c = 0.94$). This is highly suggestive that the mechanism by which the Ni 3d orbitals are distorted under strain is predominantly delocalised or non-directional. The differences between the Ni₂/Ni_{2L} and Ni₃ responses indicate that increasing the local valence of the Ni atom makes the local orbitals modestly more susceptible to distortion; however, Figure 3d–f show very clearly that these effects are minor when compared to those that are delocalised.

The effects of basal strain (variation in a) on the projected density of states (PDOS) is shown in Figure 4 for the (a) Ce 6s, (b) Ce 4f, (c–e) Ni 4s, and (f–h) Ni 3d states. The Ce 6s \uparrow (\downarrow) states show a maximum (minimum) at -2.8 eV (-1.7 eV) for the case of maximum compressive strain ($a = 4.00$ Å). These shift to lower energies, specifically at -4.0 eV (-3.5 eV) for the case of maximum tensile strain ($a = 5.00$ Å). The Ce 4f states in Figure 4b show significantly less variation with the only occupied spin-up state remaining comparatively constant at -0.5 eV. All spin down components of Ce 4f lie in the region $E - E_F > 5$ eV. A similar level of localisation is evident for the Ni 3d states. All three species have leading spin-up (spin-down) states at approximately -1.6 eV (-0.3 eV Ni₂/Ni_{2L} and -0.03 eV Ni₃). The variance in the position of the Ni 3d states is ± 0.05 eV across the range of strains considered in the current work, whereas the Ni 4s states show a variance of ± 1.0 eV.

The different variances in the peak position are typical for localised states—particularly the Ce 4f states and, to a very similar extent, the Ni 3d states—and their delocalised (s) contemporaries. In the delocalised case, the energetic variances compensate for changes in the overlap that occurs as the crystal is deformed. Consequently, the variances are greater for states that demonstrate a greater degree of delocalization—in this case, for the Ce 6s and Ni 4s states. Crystal field effects are also evident from the formation of additional electronic states that evolve as the amount of strain is varied. The development of these additional states are seen particularly for the Ni₂/Ni_{2L} 4s and Ni₃ 3d sequences shown in Figure 4c–e and Figure 4f–h, respectively. However, they are precluded from further analysis, as the focus of the paper is on the interaction between states rather than the character of individual states.

Figures 5 and 6 respectively show the bond order (BO) between all groups of Ce–Ni and Ni–Ni interactions. In the current work, BO is used as a measure of interaction strength in the same way it was used in recent studies of Ce/Pd surface alloys [24]. A positive (negative) value for BO indicates that the interaction is bonding (anti-bonding). Figure 5a shows the Ce 6s–Ni 4s interactions. The Ce–Ni₂ BO were not significantly different to the Ce–Ni_{2L} BO presented and are therefore removed for brevity. Figure 5a shows that all Ce 6s–Ni 4s interactions decrease in anti-bonding character as the in-plane lattice parameter a increases. However, the out-of-plane distortion affects the two groups of interactions differently. The Ce–Ni₃ interaction becomes increasingly anti-bonding as c increases, whereas the reverse is true for the Ce–Ni_{2L} interaction. This shows that, though the Ce–Ni₃ inter-nuclear direction is purely in-plane, its binding is strongly affected by out-of-plane distortion. A re-ordering is also seen between the Ni 4s–Ni 4s interactions in Figure 6a. This is clearly demonstrated for in the Ni₃–Ni₂ interaction; moreover, though it is also observable for Ni_{2L}–Ni₂, the effect is clearly enhanced if the inter-nuclear vector lies out of the basal plane.

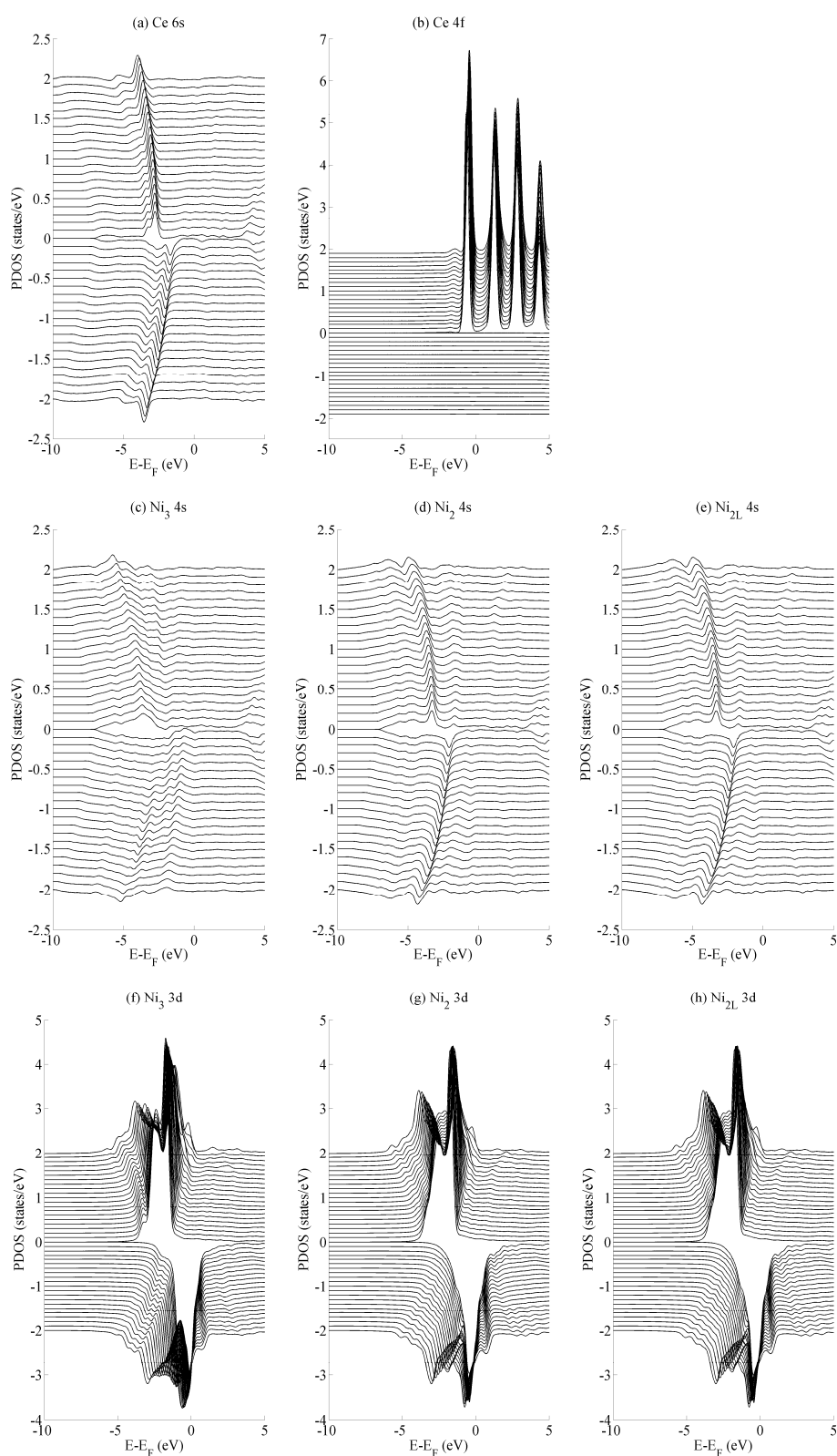


Figure 4. The effects of basal strain on the projected density of states (PDOS) of bulk CeNi_5 for the (a) Ce 6s, (b) Ce 4f, (c–e) Ni 4s and (f–h) Ni 3d states. Each panel shows spin-up and -down components in the PDOS > 0 and PDOS < 0 portions of the graph, respectively. Subsequent curves are offset vertically for clarity and were obtained using values of $a = 4.00, 4.05, \dots, 5.00$ Å. The curves obtained for $a = 4.00$ Å lie along the line PDOS = 0, and those for $a = 5.00$ Å lie furthest from this axis. For all the curves presented in this figure, $c = 0.84$.

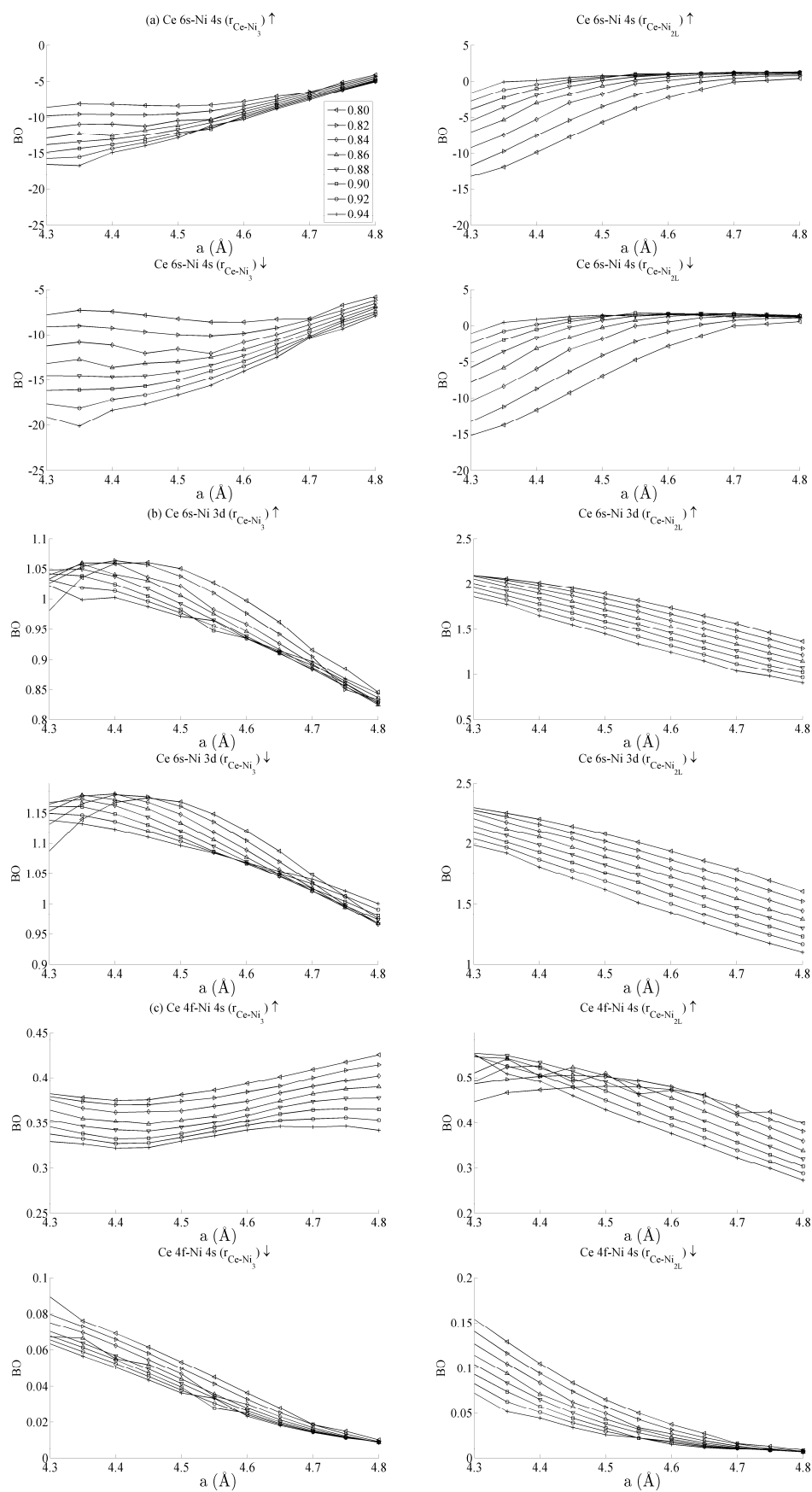


Figure 5. Cont.

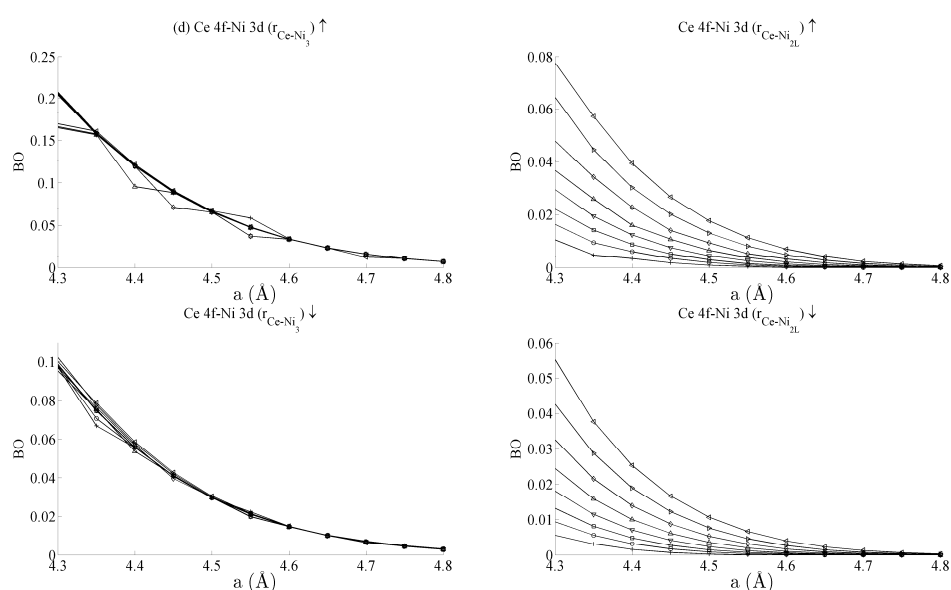


Figure 5. Bond orders (BO) of the state-resolved Ce–Ni interactions within the strained $CeNi_5$ system for the (a) Ce 6s–Ni 4s, (b) Ce 6s–Ni 3d, (c) Ce 4f–Ni 4s and (d) Ce 4f–Ni 3d interactions. The \uparrow and \downarrow arrows denote BO estimated using the spin-up and -down components of the crystal orbital overlap population (COOP), respectively. The subscripts in each panel indicate the pair of atoms between which the BO has been evaluated. The legend in (a) shows the values of c used for each curve, and the same legend applies to every panel in both Figures 5 and 6.

Figure 5b shows the BO between the Ce 6s–Ni 3d states. The interaction is bonding but there is a smaller variation in strain than was seen for the Ce 6s–Ni 4s case. This is because the Ni 3d states are more localised. This trend continues for the Ce 4f cases in Figure 5c,d. Ce 4f states lie at higher energies than the Ni 3d states and are consequently spatially more localised. Figure 5c,d thus precisely show that the bond orders become progressively smaller as the localisation increases, particularly for the group of Ce 4f–Ni 3d.

Table 1 summarises the bond order curves presented in Figure 5. In both Tables 1 and 2, the average bond order $\langle BO \rangle$ and the standard deviation of the bond order σ_{BO} were calculated using the data presented in Figures 5 and 6, across all strain states. Table 1 clearly shows that the largest variance of BO occurs between the delocalised Ce 6s–Ni 4s states with comparatively nominal changes being seen for all the remaining interactions. This trend is seen to a similar extent in Table 2, which analyses the Ni–Ni interactions presented in Figure 6a–c in the same way. In the latter case, however, stronger interactions are seen between the Ni 3d states and the other Ni states than are seen between Ce 4f and the remaining states.

Table 1. Summary of the average Ce–Ni bond order $\langle BO \rangle$ and its standard deviation σ_{BO} for the strain states of the $CeNi_5$ system defined in Figure 5. The most significant BO are highlighted.

Interaction	r	Spin	$\langle BO \rangle$	σ_{BO}
Ce 6s–Ni 4s	Ce–Ni ₃	\uparrow	–12.5	5
	Ce–Ni _{2L}	\uparrow	–5.0	6
	Ce–Ni ₃	\downarrow	–12.4	5
	Ce–Ni _{2L}	\downarrow	–5.0	6
Ce 6s–Ni 3d	Ce–Ni ₃	\uparrow	0.9	0.1
	Ce–Ni _{2L}	\uparrow	1.5	0.5
	Ce–Ni ₃	\downarrow	1.05	0.1
	Ce–Ni _{2L}	\downarrow	1.75	0.75

Table 1. Cont.

Interaction	r	Spin	$\langle BO \rangle$	σ_{BO}
Ce 4f–Ni 4s	Ce–Ni ₃	↑	0.35	0.05
	Ce–Ni _{2L}	↑	0.40	0.15
	Ce–Ni ₃	↓	0.04	0.04
	Ce–Ni _{2L}	↓	0.075	0.075
Ce 4f–Ni 3d	Ce–Ni ₃	↑	0.1	0.1
	Ce–Ni _{2L}	↑	0.05	0.03
	Ce–Ni ₃	↓	0.05	0.05
	Ce–Ni _{2L}	↓	0.03	0.03

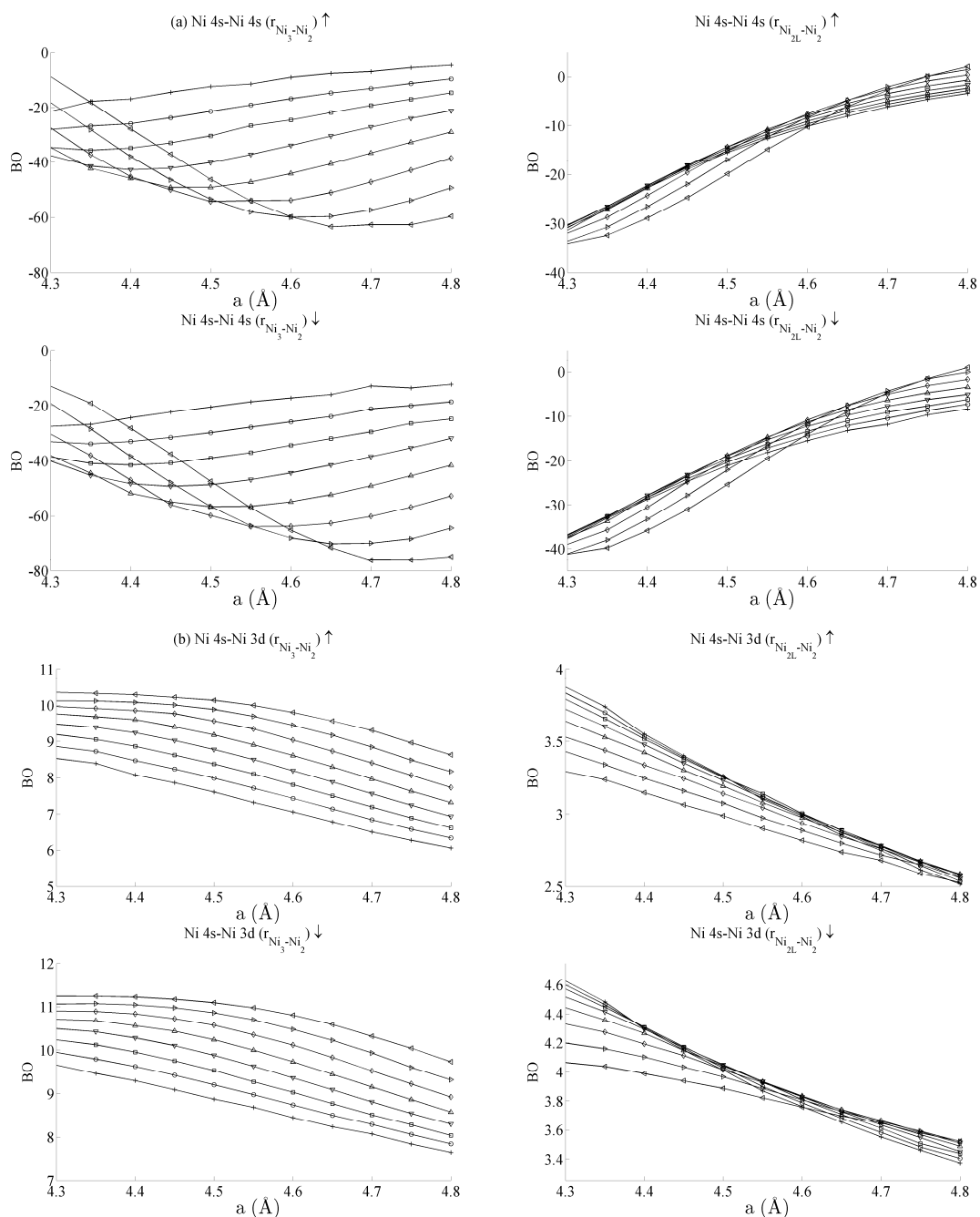


Figure 6. Cont.

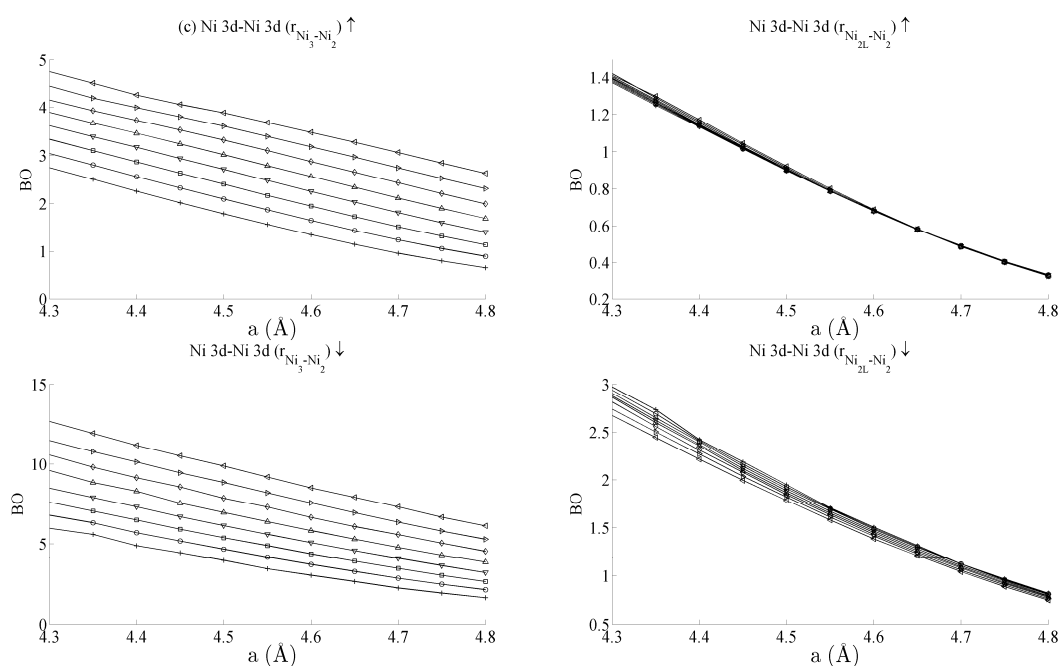


Figure 6. Bond orders (BO) of the (a) Ni 4s–Ni 4s, (b) Ni 4s–Ni 3d, and (c) Ni 3d–Ni 3d interactions within the strained CeNi₅ system. The \uparrow and \downarrow arrows denote BO estimated using the spin-up and -down components of the crystal orbital overlap population (COOP), respectively. The legend in Figure 5a defines the values of c used for each curve.

Table 2. Summary of the average Ni–Ni bond order $\langle BO \rangle$ and its standard deviation σ_{BO} for the strain states of the CeNi₅ system defined in Figure 6. The most significant BOs are highlighted.

Interaction	r	Spin	$\langle BO \rangle$	σ_{BO}
Ni 4s–Ni 4s	Ni ₃ –Ni ₂	\uparrow	–40	20
	Ni _{2L} –Ni ₂	\uparrow	–15	15
	Ni ₃ –Ni ₂	\downarrow	–40	40
	Ni _{2L} –Ni ₂	\downarrow	–20	20
Ni 4s–Ni 3d	Ni ₃ –Ni ₂	\uparrow	9	3
	Ni _{2L} –Ni ₂	\uparrow	3.25	0.5
	Ni ₃ –Ni ₂	\downarrow	10	2
Ni 3d–Ni 3d	Ni _{2L} –Ni ₂	\downarrow	4	0.6
	Ni ₃ –Ni ₂	\uparrow	3	2
	Ni _{2L} –Ni ₂	\uparrow	0.75	0.65
	Ni ₃ –Ni ₂	\downarrow	7.5	5
	Ni _{2L} –Ni ₂	\downarrow	1.75	1.25

The analysis has therefore shown that significant changes occur to the non-magnetic Ce 6s–Ni 4s interaction as the CeNi₅ crystal is strained. A weaker but significant change is also seen during strain to both the Ni 3d–Ce 6s and Ni 3d–Ni 4s, but little change occurs to the Ce 4f states. It is therefore possible to treat the localised Ni 3d and Ce 4f parts of the system separately and possible to conjecture that an RKKY-type interaction acts on the Ni 3d states because of the dependence of these states on the delocalised components of the crystal.

4. Conclusions

In the current work, the bulk CuNi₅ system was investigated using spin-polarised density functional theory (DFT) and has focussed on elucidating the behaviour of the system under strain using real space techniques. The study has shown that, during strain, the spin moment localised

on the Ni atoms changes significantly compared with those localised on the Ce atoms that remain relatively constant. The spin moment associated with both the Ni 4s and Ce 6s states has been shown to be negligible.

Changes in the delocalised Ce 6s–Ni 4s interactions during strain have been shown to be significant. This was evidenced by measuring the bond order (BO) between these two components. BO studies also show a weaker, though still significant, change between the Ni 3d and both the Ce 6s and Ni 4s states. These observations may be interpreted as evidence of an RKKY-type interaction existing between the Ni 3d states, as RKKY is typically considered as an interaction that occurs between localised spin moments via a delocalised intermediary. The pedagogy of strain engineering within DFT has therefore been demonstrated to be an effective way of elucidating this type of mechanism within a complicated magnetic system.

Acknowledgments: This work was supported by the author's membership of the UK's HEC Materials Chemistry Consortium, which is funded by the EPSRC (EP/L000202) and used the ARCHER UK National Supercomputing Service (<http://www.archer.ac.uk>).

Conflicts of Interest: The author declares no conflict of interest.

References

1. Dantzer, P. Properties of intermetallic compounds suitable for hydrogen storage applications. *Mater. Sci. Eng. A* **2002**, *329–331*, 313–320. [[CrossRef](#)]
2. Wang, J.; Jorda, J.L.; Pisch, A.; Flükiger, R. Experimental study of the CeNi₅–CeCu₅ system. *Intermetallics* **2006**, *14*, 695–701. [[CrossRef](#)]
3. Nordstrom, L.; Brooks, M.S.S.; Johansson, B. Theoretical study of the enhanced paramagnetism in CeNi_x ($x = 1, 2, \text{ and } 5$). *Phys. Rev. B* **1992**, *46*, 3458–3464. [[CrossRef](#)]
4. Gignoux, D.; Givord, F.; Lemaire, R.; Tasset, F. Thermal dependence of the susceptibility densities in CeNi₅. *J. Phys. Colloq.* **1982**, *43*, 257–261. [[CrossRef](#)]
5. Grechnev, G.E.; Logosha, A.V.; Panfilov, A.S.; Kuchin, A.G.; Vasijev, A.N. Effect of pressure on the magnetic properties of YNi₅, LaNi₅, and CeNi₅. *Low Temp. Phys.* **2011**, *37*, 138–143. [[CrossRef](#)]
6. Knyazev, Y.V.; Kuz'min, Y.I.; Kuchin, A.G. Optical properties of CeNi₅ and CeNi₄M (M = Al, Cu) compounds. *J. Alloys Compd.* **2011**, *509*, 557–559. [[CrossRef](#)]
7. Coldea, M.; Andreica, D.; Bitu, M.; Crisan, V. Spin fluctuations in YNi₅ and CeNi₅. *J. Magn. Magn. Mater.* **1996**, *157–158*, 627–628. [[CrossRef](#)]
8. Reiffers, M.; Della Mea, M.; Bauer, E.; Pristáš, G. Pressure and field effects on spin fluctuations in CeNi₅. *J. Magn. Magn. Mater.* **2004**, *272–276*, 605–607. [[CrossRef](#)]
9. Moriya, T.; Takahashi, Y. Spin fluctuations in itinerant electron magnetism. *J. Phys. Colloq.* **1978**, *39*, 1466–1471. [[CrossRef](#)]
10. Sun, Y.; Thompson, S.E.; Nishida, T. Physics of strain effects in semiconductor and metal-oxide-semiconductor field-effect transistors. *J. Appl. Phys.* **2007**, *101*, 104503. [[CrossRef](#)]
11. Fischetti, M.V.; Laux, S.E. Band structure, deformation potentials, and carrier mobility in strained Si, Ge and SiGe alloys. *J. Appl. Phys.* **1996**, *80*, 2234–2252. [[CrossRef](#)]
12. Fu, D.Y.; Zhang, R.; Wang, B.G.; Liu, B.; Xie, Z.L.; Xiu, X.Q.; Lu, H.; Zheng, Y.D.; Edwards, G. Biaxial and uniaxial strain effects on the ultraviolet emission efficiencies of Al_xGa_{1-x}N films with different Al concentrations. *J. Appl. Phys.* **2010**, *108*, 103107. [[CrossRef](#)]
13. Steel, F.M.; Tuttle, B.R.; Shen, X.; Pantelides, S.T. Effects of strain on the electrical properties of silicon carbide. *J. Appl. Phys.* **2013**, *114*, 013702. [[CrossRef](#)]
14. Shuttleworth, I.G. Controlled FCC/on-top binding of H/Pt(111) using surface stress. *Appl. Surf. Sci.* **2016**, *378*, 286–292. [[CrossRef](#)]
15. Stamenkovic, V.R.; Fowler, B.; Mun, B.S.; Wang, G.; Ross, P.N.; Lucas, C.A.; Marković, N.M. Improved Oxygen Reduction Activity on Pt₃Ni(111) via Increased Surface Site Availability. *Science* **2007**, *315*, 493–497. [[CrossRef](#)] [[PubMed](#)]
16. Soler, J.M.; Artacho, E.; Gale, J.D.; García, A.; Junquera, J.; Ordejón, P.; Sánchez-Portal, D. The SIESTA method for ab initio order-N materials simulation. *J. Phys. Condens. Matter* **2002**, *14*, 2745–2779. [[CrossRef](#)]

17. Perdew, J.P.; Ruzsinszky, A.; Csonka, G.I.; Vydrov, O.A.; Scuseria, G.E.; Constantin, L.A.; Zhou, X.; Burke, K. Restoring the density-gradient expansion for exchange in solids and surfaces. *Phys. Rev. Lett.* **2008**, *100*, 136406. [[CrossRef](#)] [[PubMed](#)]
18. Junquera, J.; Paz, Ó.; Sánchez-Portal, D.; Artacho, E. Numerical atomic orbitals for linear-scaling calculations. *Phys. Rev. B* **2001**, *64*, 235111. [[CrossRef](#)]
19. Troullier, N.; Martins, J.L. Efficient pseudopotentials for plane-wave calculations. *Phys. Rev. B* **1991**, *4*, 1993–2006. [[CrossRef](#)]
20. Troullier, N.; Martins, J.L. Efficient pseudopotentials for plane-wave calculations. II. Operators for fast iterative diagonalization. *Phys. Rev. B* **1991**, *43*, 8861–8869. [[CrossRef](#)]
21. Kleinman, L.; Bylander, D.M. Efficacious form for model pseudopotentials. *Phys. Rev. Lett.* **1982**, *48*, 1425–1428. [[CrossRef](#)]
22. Moreno, J.; Soler, J.M. Optimal meshes for integrals in real- and reciprocal-space unit cells. *Phys. Rev. B* **1992**, *45*, 13891–13898. [[CrossRef](#)]
23. Petukhov, A.G.; Mazin, I.I.; Chioncel, L.; Lichtenstein, A.I. Correlated metals and the LDA + U method. *Phys. Rev. B* **2003**, *67*, 1531061–1531064. [[CrossRef](#)]
24. Shuttleworth, I.G. The magnetic properties of Ce/Pd surface alloys investigated using DFT. *Chem. Phys. Lett.* **2014**, *605–606*, 5–9. [[CrossRef](#)]
25. Hirshfeld, F.L. Bonded-atom fragments for describing molecular charge densities. *Theor. Chim. Acta* **1977**, *44*, 129–138. [[CrossRef](#)]
26. Guerra, C.F.; Handgraaf, J.-W.; Baerends, E.J.; Bickelhaupt, F.M. Voronoi deformation density (VDD) charges: Assessment of the Mulliken, Bader, Hirshfeld, Weinhold, and VDD methods for charge analysis. *J. Comput. Chem.* **2004**, *25*, 189–210. [[CrossRef](#)] [[PubMed](#)]
27. Bickelhaupt, F.M.; Van Eikema Hommes, N.J.R.; Guerra, C.F.; Baerends, E.J. The carbon-lithium electron pair bond in $(\text{CH}_3\text{Li})_n$ ($n = 1, 2, 4$). *Organometallics* **1996**, *15*, 2923–2931. [[CrossRef](#)]
28. Dronskowski, R.; Blöchl, P.E. Crystal Orbital Hamilton Populations (COHP). Energy-Resolved Visualization of Chemical Bonding in Solids based on Density-Functional Calculations. *J. Phys. Chem.* **1993**, *97*, 8617–8624. [[CrossRef](#)]
29. Shuttleworth, I.G. Comparative investigation of the $c(2 \times 2)$ -Si/Cu(011) and $(\sqrt{3} \times \sqrt{3})R30^\circ$ -Cu₂Si/Cu(111) surface alloys using DFT. *Appl. Surf. Sci.* **2012**, *258*, 3475–3484. [[CrossRef](#)]
30. Butler, B.; Givord, D.; Givord, F.; Palmer, S.B. The elastic constants of CeNi₅. *J. Phys. C Solid State Phys.* **1980**, *13*, L743–L746. [[CrossRef](#)]



© 2016 by the author; licensee MDPI, Basel, Switzerland. This article is an open access article distributed under the terms and conditions of the Creative Commons Attribution (CC-BY) license (<http://creativecommons.org/licenses/by/4.0/>).